Strength-ductility synergy through microstructural and compositional heterogeneity in directed energy deposition additive manufacturing of face-centered cubic materials

Md.R.U. Ahsan, Nadim S. Hmeidat, Saiful Islam, Xuesong Fan, Jonathan D. Poplawsky, Peter K. Liaw, Yousub Lee, Brett G. Compton, Yongho Jeon, Duck Bong Kim

PII: S2238-7854(24)02522-5

DOI: https://doi.org/10.1016/j.jmrt.2024.10.253

Reference: JMRTEC 12155

To appear in: *Journal of Materials Research and Technology*

Received Date: 24 September 2024

Revised Date: 29 October 2024

Accepted Date: 30 October 2024

Please cite this article as: Ahsan MRU, Hmeidat NS, Islam S, Fan X, Poplawsky JD, Liaw PK, Lee Y, Compton BG, Jeon Y, Kim DB, Strength-ductility synergy through microstructural and compositional heterogeneity in directed energy deposition additive manufacturing of face-centered cubic materials, *Journal of Materials Research and Technology*, https://doi.org/10.1016/j.jmrt.2024.10.253.

Strength-ductility synergy through microstructural and compositional heterogeneity in directed energy deposition additive manufacturing of face-centered cubic materials

Md. R. U. Ahsan[a], Nadim S. Hmeidat[b], Saiful Islam[a], Xuesong Fan[c], Jonathan D. Poplawsky[d], Peter K. Liaw[c], Yousub Lee[e], Brett G. Compton[c,f], Yongho Jeon[g,**], and Duck Bong Kim[h,*]

[a] Department of Mechanical Engineering, Tennessee Technological University, Cookeville, TN 38505, United States
[b] Manufacturing Science Division, Oak Ridge National Laboratory, Oak Ridge, TN 37932, United States
[c] Department of Materials Science and Engineering, University of Tennessee, Knoxville, TN 37996, United States
[d] Center for Nanophase Materials Sciences, Oak Ridge National Laboratory, Oak Ridge, TN 37830, United States
[e] Computational Sciences and Engineering Division, Oak Ridge National Laboratory, Oak Ridge, TN 37830, United States
[f] Mechanical, Aerospace, and Biomedical Engineering Department, University of Tennessee, Knoxville, TN 37996, United States
[g] Department of Mechanical Engineering, Ajou University, Suwon, Gyeonggi-do, South Korea
[h] Department of Manufacturing and Engineering Technology, Tennessee Technological University, Cookeville, TN 38505, United States

[**]Co-corresponding author: Y. Jeon, e-mail address: princaps@ajou.ac.kr
[*]Corresponding author: D.B. Kim, e-mail address: dkim@tntech.edu

Abstract

Directed energy deposition (DED) is an additive manufacturing (AM) process based on welding technology and offers the advantages of large build volume, high deposition rate, and ability to fabricate multi-material parts. Epitaxial continuous columnar grain growth is a characteristic microstructural feature of DED processed alloys. In this study, a bamboo-like microstructure (periodic alternation of equiaxed and columnar structure) was produced by adopting an intermittent deposition strategy in 316L stainless steel and Inconel 625. The formation of a bamboo-like alternating microstructure was confirmed through electron backscattered diffraction (EBSD) analysis. Hardness mapping showed that the columnar to equiaxed transition (CET) occurred at the region right below the fusion line. A finite element (FE) model was used to investigate the relationship between the temperature gradient (G) and the solidification rate (R). The FE model showed a low G/R ratio at the region right below the interface promoting the CET. The grain size and material-dependent deformation behaviors are analyzed using digital image correlation (DIC). The lower deformation on the fine-grain regions observed in DIC analysis is attributed to a higher strain hardening rate, which is confirmed through dislocation density analysis on a tensile-interrupted specimen. The periodically alternating grain size coupled with the microstructural changes caused by intermittent deposition strategy result in a better strength-ductility synergy in both single-material and bimetallic specimens.

Keywords: Directed energy deposition (DED), Grain morphology, Deformation mechanisms, Dislocation density.

1. Introduction

Additive manufacturing (AM) presents new possibilities for the design and fabrication of metallic components with complex geometries in aerospace, energy, and biomedical applications [1]. AM technology promises potential in part cost reduction by reducing material waste and time to market [2]. In addition, AM enables an increase in freedom of design, potentially saving weight and facilitating the manufacture of complex assemblies as a single component [3]. Along with the aforementioned advantages, AM techniques offer added flexibility in varying the composition and microstructure across different spatial dimensions, and thereby enabling the creation of functionally graded structures with locally adapted tailored performance [4]. Therefore, a significant amount of research has been reported on the fabrication of compositionally graded structures based on various powder based directed energy deposition (DED) techniques [5-8].

In this regard, Wire-arc DED also known as wire-arc additive manufacturing (WAAM), has evolved as an alternative manufacturing route which has the potential to fabricate large-scale metal parts with low material and equipment cost, higher material utilization, and lower environmental impact [4]. The WAAM process also exhibits flexibility with materials and can be used for fabricating compositionally graded structures [9,10]. Several research projects have reported functionally graded structures fabricated with conventional (e.g., austenitic stainless-steel SS316L) and superalloys (e.g., Inconel625) using Gas metal arc welding (GMAW)-WAAM [11] to achieve tailored properties suitable for different industries. In this regard, bimetallic additively manufactured structures (BAMS) of SS316L and In625 can complement each other to achieve cost-effective solutions without compromising performance. This approach is evident in oil-reformer towers, where Inconel dampers withstand 1000°C and corrosive environments, while austenitic stainless-steel axles operate in lower-temperature conditions. In addition, nickel-based alloy coatings are commonly applied to stainless steel to provide durable protection against corrosion, wear, and high-temperature damage; thereby extending component lifespan and reducing maintenance costs [9]. Abe and Sasahara [12] successfully fabricated a defect-free BAMS through sequential deposition of austenitic stainless steel and a nickel-based alloy using the GMAW-WAAM process. The interface between the two materials exhibited a sharp compositional gradient. In prior works, the authors fabricated BAMS of SS316L and Inconel 625 (In625) [9]. Although the study primarily focused on the bimetallic interface, further investigation of the individual materials would provide a more comprehensive understanding of the overall mechanical behavior.

Despite having numerous advantages in AM, the presence of columnar morphology in the microstructure has been widely reported in various studies for different materials [13-17], which often results in poor mechanical performance along the grain growth direction. The formation of columnar or equiaxed grains is primarily influenced by the thermal gradient (G) to solidification rate (R) ratio [18]. Different G/R ratios can be

achieved in laser-powder bed fusion (PBF) to tailor the columnar to equiaxed transition (CET) of the microstructure by controlling the process parameters [19]. Morton et al. [20] tailored the microstructure of Ti6Al4V using a beam-scanning strategy with electron beam melting (EBM)-AM and achieved a significantly improved fatigue performance (~22% increase) through microstructural grading [20. Raghavan et al. [21] showed that maintaining an equiaxed microstructure in EBM requires scaling the energy density with respect to the cross-sectional area, with increased energy density leading to an equiaxed microstructure in the deposit. Popovich et al. [22] reported achieving transitions in microstructure, texture, and properties of Inconel 718 in selective laser melting (SLM) by controlling the process parameters, and they also observed a difference in local strain due to grain size heterogeneity.

Epitaxial growth of large columnar grains across multiple layers is commonly observed in WAAM [23], which often results in anisotropic mechanical properties [24,25]. However, some studies regarding GMAW have reported the formation of columnar grains at the fusion zone and equiaxed grains at the heat-affected zone below the fusion line (FL) [26,27]. The underlying mechanisms responsible for the CET during solidification have been explained in prior research [28,29]. The transition between these microstructures is a function of alloy thermodynamics as well as local thermal conditions [30]. By manipulating these thermal conditions through varied process parameters, favorable solidification conditions for CET can be achieved [30]. Thus, the WAAM process has the potential to control grain morphology by manipulating thermal profiles and achieving location-specific columnar or equiaxed microstructure. This characteristic can promote tailored mechanical properties in WAAM fabricated components.

The authors' previous research [10,13,31,32], which utilized a continuous deposition strategy (CDS), reported the formation of large columnar grain growth across multiple layers. CDS can lead to temperature build-up and a slower cooling rate, particularly at the top layers. This may lead to a heterogeneous thermal history and form an inconsistency in microstructure and mechanical properties along the build direction. However, if a layer is allowed to cool down before depositing the successive one, which is known as intermittent deposition strategy (IDS), an interrupted grain growth could be observed. This can lead to a difference in hardness value measured at the interfaces and interlayer region compared to the CDS strategy [33]. In general, the IDS eliminates the temperature build-up issue and promotes a consistent thermal history in all layers. In addition, a favorable G/R ratio can be achieved near the FL to promote CET through IDS. Thus, the authors aim at interrupting the epitaxial grain growth and achieving a periodically alternating microstructure of large columnar grain and fine grain in WAAM deposited structure consisting of austenitic stainless steel (SS316L) and Inconel 625 (In625).

Therefore, the objective of the present research is firstly to investigate the CET mechanism through IDS and achieve a microstructural grading in WAAM of two face-centered-cubic (FCC) alloys: SS316L and In625. By introducing grain size heterogeneity at regular intervals through an IDS, we aim to fabricate an alternating microstructure of large columnar grain and fine grain (bamboo-like structure) with an improved strength-ductility synergy. Secondly, we intend to combine microstructural and compositional grading through the sequential deposition of In625 on top of SS316L and compare the performance enhancement. The microstructures, mechanical properties, and deformation behaviors of both single materials (SS316L

and In625) and bimetallic specimens are characterized using optical and electron microscopy, electron backscattered diffraction (EBSD), and tensile test coupled with digital image correlation (DIC). Later, the microstructural and DIC analysis results are correlated with hardness maps and EBSD analysis results of tensile-interrupted specimens. The authors also incorporated finite element analysis to numerically calculate the G/R ratio and study its influence on the formation of location specific microstructure. Finally, a comparison of mechanical properties between homogeneous and microstructurally graded SS316L, In625, and bimetallic specimens is presented to signify the performance improvement with the IDS.

2. Experiments

2.1. Materials, process, and deposition parameters

The experiments for the present work were performed on a GMAW-WAAM system consisting of a Fanuc ArcMate-100iB robot, and a Fronius TransPuls Synergic 4000MV R cold metal transfer (CMT) advanced machine with a VR7000 wire feeder unit was also used. Commercially available welding consumables of SS316L and In625 with the composition listed in **Table 1** were used as feedstock. Materials-specific process parameters with identical travel speed and wire-feed speed were used in this study to maintain a constant deposition rate. The process parameters are summarized in **Table 2**. A solid cube having a size of 60 mm × 60 mm × 135 mm was deposited on a low-carbon-steel substrate using wires of SS316L and In625 alloy.

Table 1: Chemical composition [weight percent (wt.-%)] of wires utilized during the experiments [9].

	%C	%Mn	%Si	%S	%P	%Cr	%Mo	%Nb+Ta	%Cu	%Fe	%Ni	Total
SS316L	0.02	2.1	0.81	0.01	0.02	18.9	2.2	-	0.23	Balance	11.8	100%
In625	0.02	0.1	0.14	0.001	0.005	21.7	8.5	3.8	0.23	0.4	Balance	100%

Each of weld beads was deposited layer-wise within the xy-plane, maintaining a 50% overlap between adjacent beads, each approximately 7 mm in width, **(Figure 1(a))**. The deposition pattern was rotated on the *xy*-plane by 90° in a counter-clockwise direction for the subsequent layers [9]. A 3 mm vertical offset was used between layers. The tool path is presented schematically in **Figure 1(b)**. Forty-five layers were deposited, including 23 layers of SS316L and 22 layers of In625. To promote intermittent grain growth as well as to provide consistency of thermal history, interpass temperature of 200 °C was maintained during the deposition of each layer. A thermocouple of the k-type was used to measure the surface temperature. Utilizing the deposition parameters which are explained in detail in the study [9], a cube-shaped solid bimetallic structure was fabricated as shown in **Figure 1(c)**.

Table 2: Deposition parameters of SS316L and In625 [9].

	Variables	SS316L	In625
Deposition parameters	WAAM Process	CMT	CMT
	Current (A)	200	148
	Voltage (V)	13.1	14.5
	Moving speed (mm/min.)	600	600
	Layer thickness (mm)	3	3

x and *y* offset (mm)	3.5	3.5
Bead overlap (%)	50	50

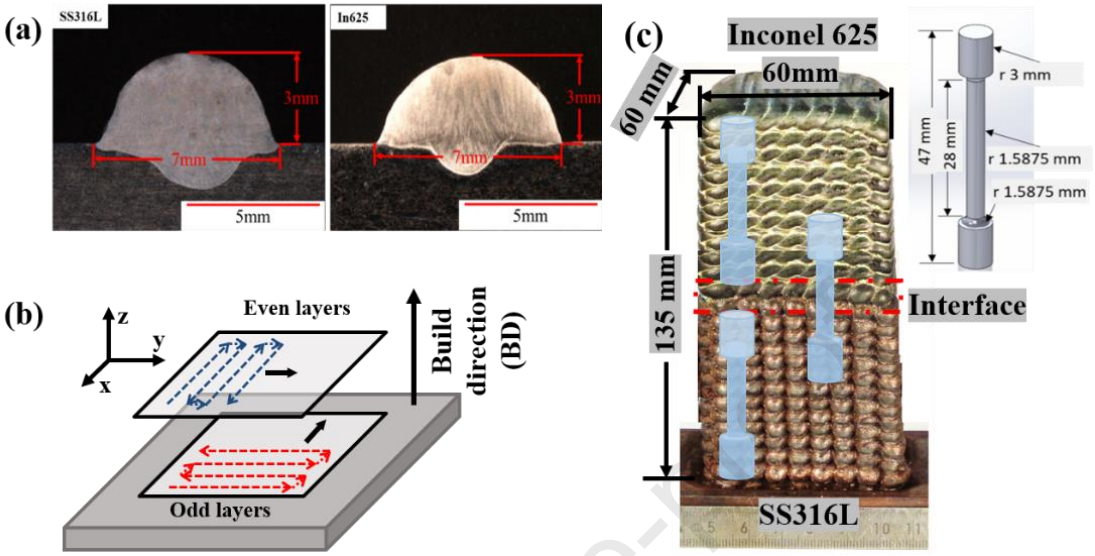

Figure 1. (a) Bead cross-section on the *yz* plane with measurements from single-layer deposits of SS316L and In625 [9], (b) schematic representation of the arc movement [9], and (c) the fabricated bimetallic structure of SS316L and In625 with the dimensions and location of the tensile test specimens.

2.2. Sample preparation and analysis

For microstructural analysis, specimens were prepared from the SS316L, In625, and the bimetallic interface having a cross-section on the *yz*-plane. Microstructure characterization specimens were then ground and polished, following the standard metallography technique [34]. Glyceregia and diluted aqua regia etchants were utilized for SS316L and In625, respectively, to reveal the microstructural features. Optical microscopy (OM), scanning electron microscope (SEM), and energy-dispersive X-ray spectroscopy (EDS) techniques were used for the microstructure, composition, and fracture morphology analyses which are described in detail in a previous study [9]. For a more accurate compositional analysis, atom probe tomography (APT) was used. APT specimens were prepared using an FEI Nova 200 dual beam SEM/focused ion beam (FIB) by lifting out triangular prism wedges from the sample, mounting sections of the wedge onto Si microtip array posts, sharpening and cleaning following the method described by Thompson et al. [35]. The APT experiments were run using a CAMECA LEAP 4000XHR in laser mode with a 30K base temperature, 70-80 pJ laser power, 0.5% detection, and 200 kHz pulse repetition rate. Data reconstruction and analysis were performed using the IVAS 3.8 software package. Four APT datasets were analyzed from two different lift-out locations. EBSD analysis was conducted on non-deformed and partially strained tensile-interrupted specimens, utilizing a Zeiss EVO MA15 machine equipped with a Bruker eFlash EBSD detector. Subsequently, EBSD data analysis was performed using ATEX software [36].

Tensile properties were investigated using MTS 810 servo-hydraulic machine. The tensile samples were machined out using wire electric discharge machining (wire-

EDM), in accordance with the American Society for Testing and Materials (ASTM) E8 standard [37] with dimensions shown in **Figure 1** [9]. Microhardness tests were performed on a Buehler Wilson VH 1202 on a Vickers scale with a 500 g load.

2.3. Digital image correlation

Uniaxial tensile tests coupled with DIC analysis were performed on a universal MTS servo-hydraulic load frame having a 25 *kN* interface load cell. Gripping pressure of 500 psi was utilized for all tested specimens. A 3D DIC system (Correlated Solutions, Inc) was employed during these uniaxial tests to analyze local deformation fields (**Figure 2(a)**). Random black-on-white speckle patterns were applied to the tensile specimens (**Figure 2(b)**). The cameras used were CSI – 2.3 MP Schneider Kreuznach Xenoplan (1.9/35-0901) and Schneider Kreuznach Cinegon (1.4/12-0906), with optics lens focal lengths of 30 mm. Maintaining a constant strain rate of 10^{-3} s^{-1}, tensile tests were carried out at room temperature following ASTM standard E8/E8M-6 [37]. To capture the strain during the experiment, images were taken matching the data acquisition rate of 5 frames per second. VIC-Snap and VIC-3D (Correlated Solutions, Inc.) software had been utilized for capturing and post processing of the images. For calibration, a 7.12 mm × 7.12 mm grid of 9 × 9 dots and 0.89 mm pitch size was used. The subset dimension was 29 × 29 pixels with a 7-pixel step size for image analysis. To improve the balance between capturing small details and overall displacement, a special filter (15-pixel Gaussian smoothing decay filter) was applied during analysis. Two types of strain were calculated from the measured displacements: Lagrangian strain and logarithmic Hencky strain.

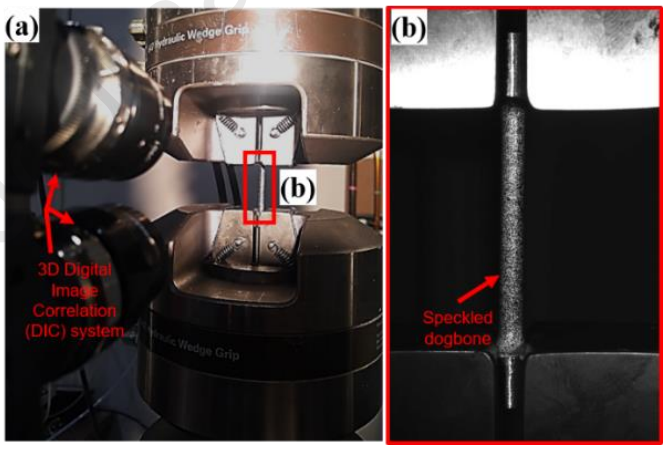

Figure 2. (a) Experiment setup for digital image correlation (DIC) and (b) representative optical image of a dog-bone specimen with a black-on-white spackle pattern.

2.4. Finite element modeling of the thermal behavior

To understand the heat transfer behavior as well as to calculate the *G*/*R* ratio of the WAAM deposits in correlation with location-specific microstructure, finite element (FE) numerical analysis was performed on a 3D model using the commercial ANSYS software (2022 R1). A moving heat source expressed as Gaussian distribution was applied to the geometry top surface (**Figure 3**). The external sides of the substrate and the deposit were subjected to both convection and radiation. The initial top surface

temperature was set at 200 °C to replicate the interpass temperature used in the experiment. The heat source travel speed was in accordance with the deposition condition. The temperature variation was obtained in each time step from the numerical model.

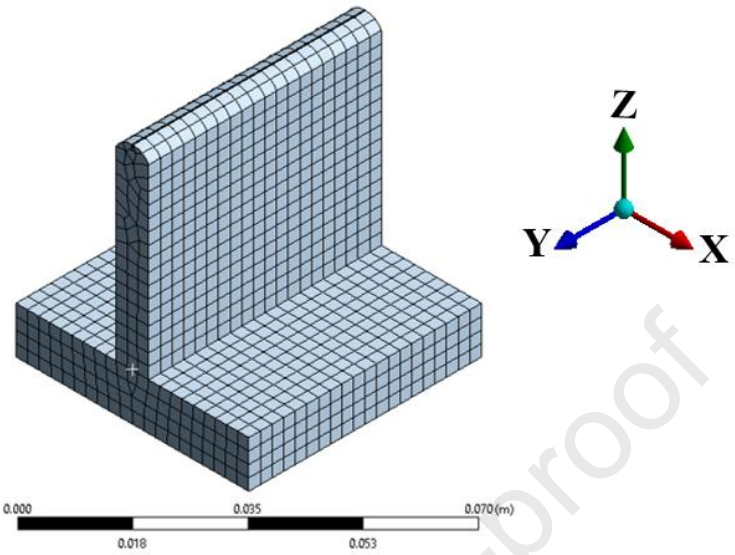

Figure 3. FE model geometry with associated mesh.

The temperature distribution $T(x,y,z,t)$ in the FE model can be obtained from the following equation [38,39]:

$$\rho C_p \frac{\partial T}{\partial t} = \frac{\partial}{\partial x}\left(k\frac{\partial T}{\partial x}\right) + \frac{\partial}{\partial y}\left(k\frac{\partial T}{\partial y}\right)\frac{\partial}{\partial z}\left(k\frac{\partial T}{\partial z}\right) + Q \quad \text{..... Eq. 1}$$

where T is node temperature, k is the thermal conductivity of the material, ρ and C_p are the density and specific heat of the material, respectively. Q represents the power generated per unit volume.

Heat transfer occurs to the surrounding environment in three heat transfer modes: conduction, convection, and radiation. The boundary condition for heat transfer is presented as [38]:

$$q_{conduction} = q(x,y,z) - q_{convection} - q_{radiation} \quad \text{..... Eq. 2}$$

Where the heat transfer through conduction $q_{conduction}$, convection $q_{convection}$, and radiation $q_{radiation}$ are expressed as follows [38]:

$$q_{conduction} = -k\Delta T \quad \text{..... Eq. 3}$$

$$q_{convection} = h_c(T - T_0) \quad \text{..... Eq. 4}$$

$$q_{radiation} = \sigma\varepsilon(T^4 - T_0^4) \quad \text{..... Eq. 5}$$

Where k is the thermal conductivity of the material, h_c is the heat convection coefficient, σ is the Stefan-Boltzman constant (5.68×10^{-8} $Wm^{-2}K^{-4}$), and ε is the surface emissivity. T and T_0 are the temperature of the molten pool and the room temperature, respectively.

The convection and radiation boundary conditions are applied on external surfaces, except for the bottom. As the bottom surface is in direct contact with a large thermal

mass (welding bed), which does not exhibit any significant fluctuation of temperature during WAAM, a constant temperature (room temperature: 25 °C) is assigned to this surface.

From this FE model, the temperatures at different locations along the *z*-axis are recorded at the same instant and used for later calculations. The *G* is calculated as follows:

$G = \frac{\partial T}{\partial d}$ …… Eq. 6

The solidification parameter *R* is closely related to the cooling rate (R_C) and *G*. The correlation between these three factors is expressed as:

$R_c = G \times R$ …… Eq. 7

The cooling rate is also calculated from the FE model using the following equation:

$R_c = \frac{\partial T}{\partial t}$ …… Eq. 8

Based on Eq. 6-8, the solidification parameter *R* can be expressed as:

$R = \frac{1}{G} \times \frac{\partial T}{\partial t}$ …… Eq. 9

3. Results

3.1. Microstructure characterization

The microstructure analysis results from OM and SEM as well as the compositional analysis from EDS for SS316L and In625 are presented in **Figure 4**. The SS316L side (**Figure 4(a)**) shows the formation of dendritic delta (*δ*)-ferrites in an austenite matrix. The elongated appearance of the dendrites is attributed to the directional cooling which is frequently observed in WAAM [11,40] and other AM techniques [13]. In the OM image, the layer interface is also prominently apparent. Observation of the microstructure at a higher magnification reveals two different types of *δ*-ferrite morphologies. At a location away from the interface, the *δ*-ferrites are primarily skeletal. However, at the layer interface, a significant amount of lathy ferrite is observed above the FL, within the subsequent deposited layer. The observed microstructures suggest a ferritic-austenitic (FA) type of solidification [41], in which austinites form through a peritectic-eutectic reaction. During cooling through the *δ*-ferrite + austenite field, the ferrite transforms into austenite until the ferrite becomes enriched in Cr and Mo, and reduced in austenite-stabilizing elements (Ni) [42]. The elemental mapping results in **Figure 4(b)** support this mechanism, showing higher Cr and Mo concentrations in *δ*-ferrites and lower Ni content in the austenite matrix. The *δ*-ferrites have a vermicular morphology in the austenite matrix.

The OM results on In625 (**Figure 4(c)**) also show primary dendritic growth with an identifiable layer interface. The higher magnification micrographs show a difference in secondary dendritic arm spacing (SDAS) between the locations near and far from the interface, with higher SDAS values at regions away from the layer interface, suggesting a slower cooling rate [43]. Almost no secondary dendrites are observed right above the FL whereas, fewer secondary dendrites with lower SDAS values are observed right below the FL, suggesting a relatively faster cooling rate in these regions [43]. The backscattered electron (BSE)-SEM micrographs of In625 show the presence

of the *γ*-austenite and Laves phase, displayed in **Figure 4(d)**. Laves phase is undesirable due to its ability to decrease the strength and increase the brittleness by depleting Nb in the alloy matrix. Details of their formation mechanism have been explained in authors' previous study [9].

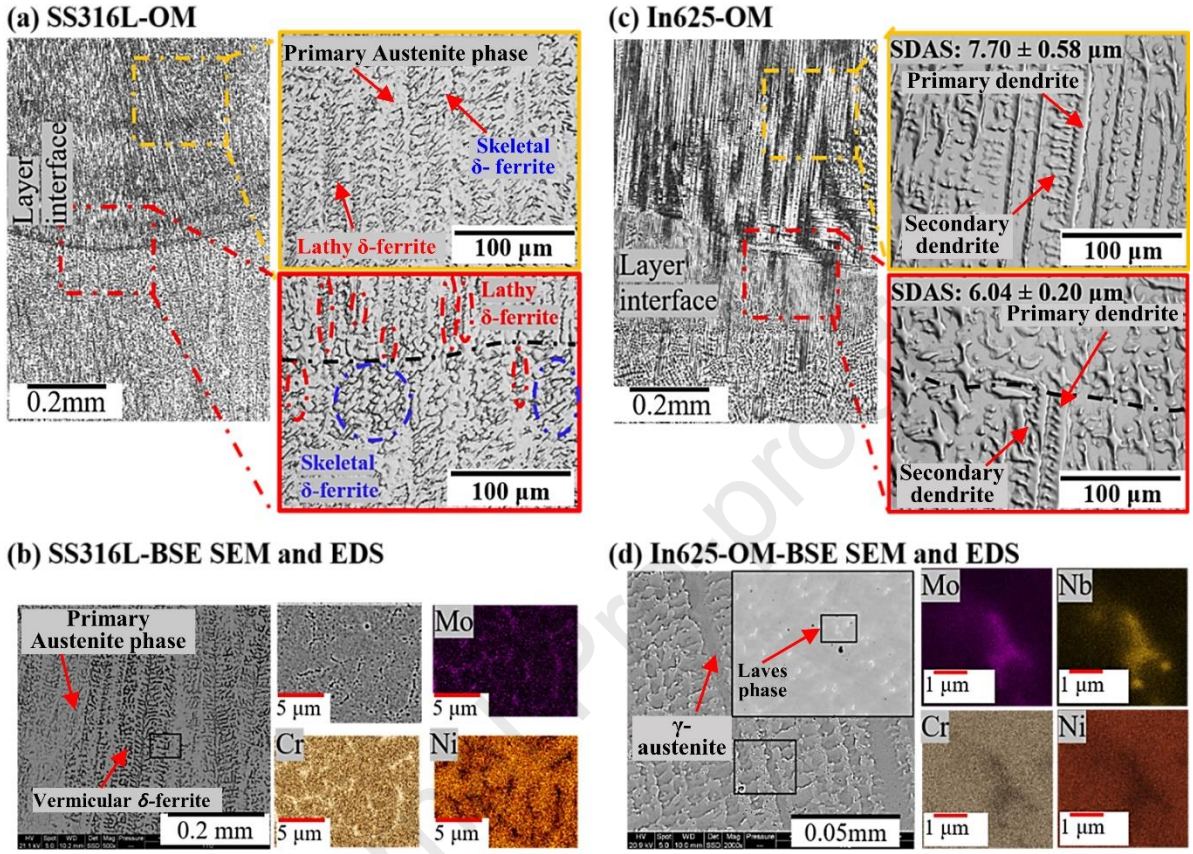

Figure 4. Microstructure and compositional results from OM and SEM analysis on (a-b) SS316L and (c-d) In625 sides.

The microstructure and compositional analysis data on the bimetallic interface are presented in **Figure 5**. The bimetallic interface is visible from the OM and BSE-SEM images. The EDS line scan data across the interface shows a transition of Fe and Ni content while the Cr content remains almost homogeneous. The sharp transition of Fe and Ni content identifies the interface. To investigate segregation at the bimetallic interface at the atomic scale, APT needle specimens were prepared from the interface, and the data are presented in **Figure 5(c)**. The APT data show a homogeneous distribution of all elements. This was validated by repeating the analysis in five different specimens. All the specimens provided similar results. Therefore, it is hypothesized that the apparent abrupt change in the composition observed in EDS is spread over a larger area, compared to nanoscale in APT. Hence, the APT specimen shows a homogeneous composition of elements.

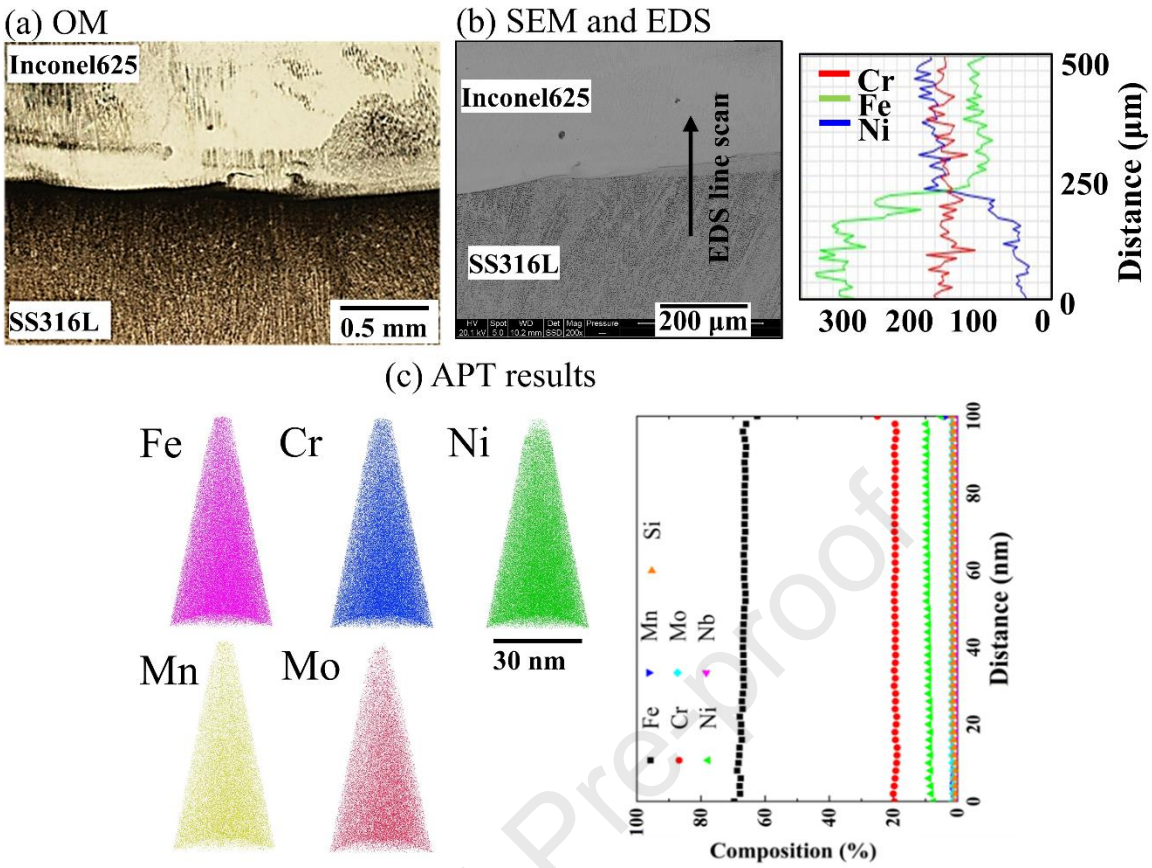

Figure 5. Microstructure and compositional analysis results on the bimetallic interface from (a) OM, (b) SEM and EDS, and (c) APT.

3.2. Grain size, morphology, and texture in IDS

To reveal the crystallography and morphology of the grains, EBSD analysis was conducted along *yz*-planes on the SS316L side, bimetallic interface, and In625 side. **Figure 6(a-c)** displays EBSD data, including pole figures, inverse pole figures (IPF), and IPF maps along build direction (BD). In cubic crystals (FCC and BCC), the primary dendrites typically develop along <001> crystallographic orientations [9]. The presence of strong texture in the <001> direction (parallel to BD) is also confirmed by the BD-IPF in **Figure 6(a-c)-(iii)**. Although the pole figures show the strongest intensity along the <001> direction, the somewhat scattered nature of the intensity signifies random rotation of the grains about the BD [25]. It should be noted that the bimetallic specimen in **Figure 6(b)** appears to have a continuous grain growth, and the bimetallic interface cannot be identified from the EBSD results. As the primary phase on both materials is FCC with the same preferred grain-growth orientation, the lattice parameters are almost identical [9], which consequently prevents the EBSD detector from identifying the two materials separately.

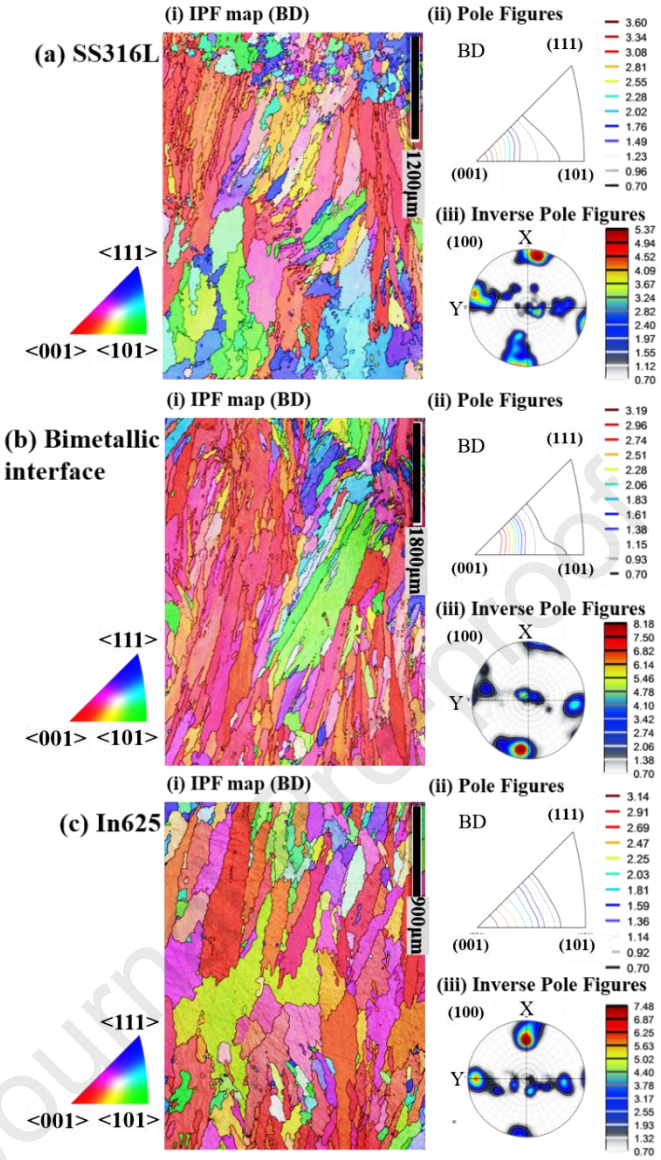

Figure 6. (i) Inverse Pole figure (IPF) maps, (ii) Pole figure, and (iii) Inverse Pole Figures (IPFs) for (a) SS316L, (b) bimetallic interface, and (c) In625.

The EBSD grain maps demonstrate the change in morphology and grain size at different locations in **Figure 7(b)**. The results indicate that the SS316L side has comparatively finer grains at two ends and large columnar grains in the interlayer region as indicated by black and red regions respectively. The bimetallic interface is not identifiable from the EBSD grain maps. This is attributed to the similarity of crystal structure and proximity of lattice parameters [9]. On the In625 side, although comparatively equiaxed grains are not observed, the grains at the layer interfaces are found to be smaller whereas the grains in the interlayer region are large and columnar as indicated by green and blue regions respectively.

To quantitatively express the location-dependent grain size and morphology, the grain size distribution is quantified from the fine grain (FG) regions (layer interface), and the large-columnar grain (CG) regions. The grain size distribution results are graphically presented in **Figure 7(c)**. The SS316L-FG-region has the smallest grains, averaging 169.63 μm. The SS316L-CG-region has large columnar grains about 416 μm in size

on average as shown in **Figure 7(c)-(ii)**. On the In625 side, the grains at the FG region are significantly larger compared to the SS316L, having an average size of approximately 290 µm. However, the grains in the CG region are significantly larger, reaching an average size of 695 µm. Notably, the In625 has a significantly larger grain size than SS316L when compared between similar locations. This might be related to the effect of heat accumulation on the substrate and previously deposited layers. Since In625 is deposited above SS316L, the preheated substrate and deposited structure promote a slower cooling rate. Consequently, this causes the formation of coarser grains. Nevertheless, in both materials, the layer interface has relatively smaller grains compared to the interlayer region.

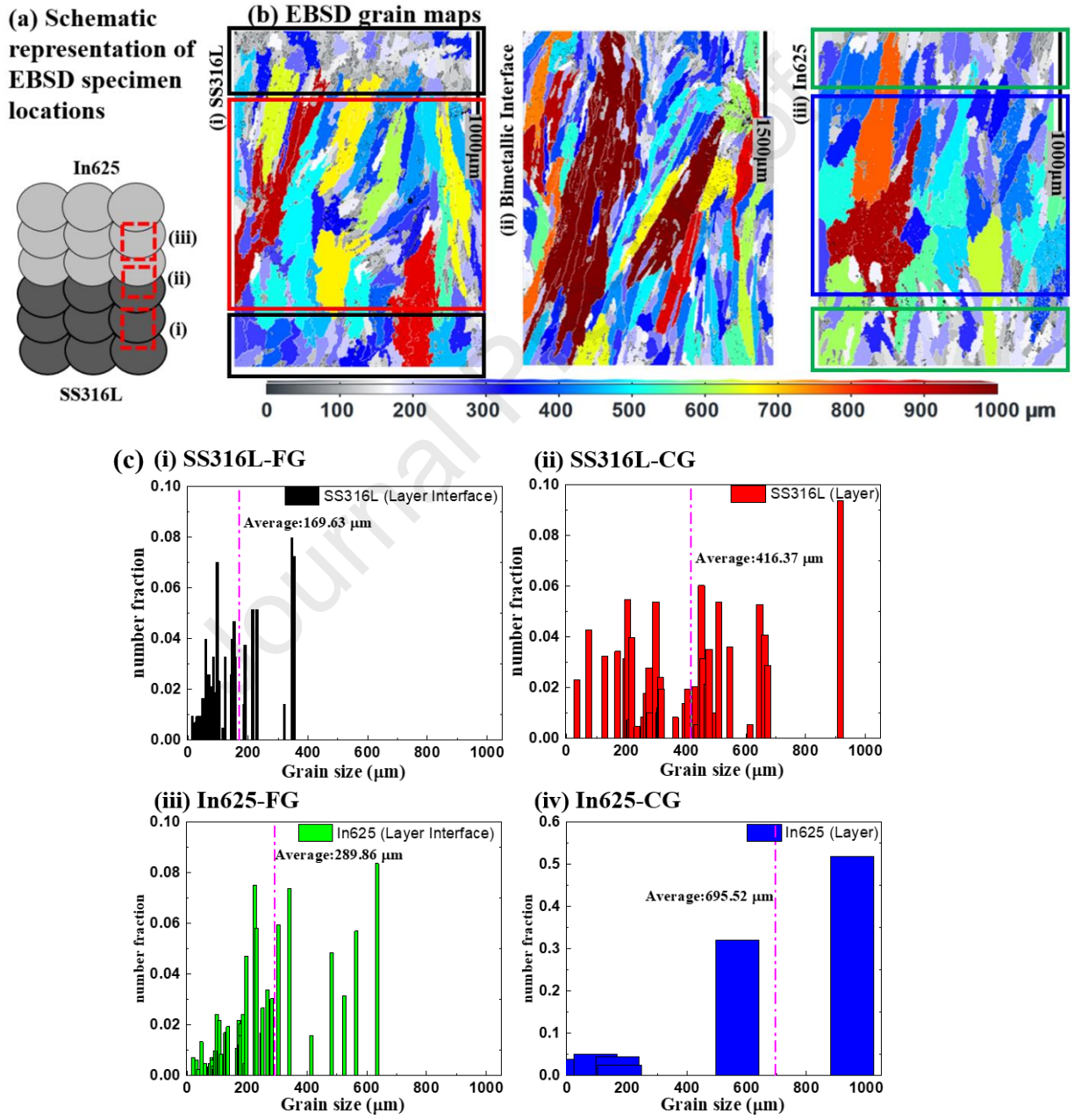

Figure 7. (a) Schematic representation of EBSD analysis locations; (b) EBSD grain maps for (i) SS316L, (ii) bimetallic interface, and (iii) In625; (c) Location-specific

grain size distribution on the (i) SS316L- FG, (ii) SS316L- CG, (iii) In625- FG, and (iv) In625- CG.

3.3. Mechanical properties

To understand the effect of microstructural and compositional heterogeneity on mechanical performance, microhardness tests were conducted at the interlayer region and layer interface of SS316L and In625. The average microhardness on the CG and FG-regions of SS316L and In625 as well as at the bimetallic interface is presented in **Figure 8**. Although both materials have similar hardness values, the FG regions are slightly harder than the CG regions. The hardness of SS316L is measured between 185 to 203 HV, consistent with previous research [5]. For In625, the hardness value ranges from 190 to 248 HV, which also agrees with other research on welded [44] and as-deposited AM In625 [12,45]. Notably, at the layer interfaces (FG regions), a higher variation in hardness is observed. These fluctuations in the hardness are attributed to the abrupt change in microstructure and grain size within a narrow area close to the FL. In contrast, the CG regions cover a larger area with similar grain size and microstructure, leading to a more uniform hardness value in this region for both materials.

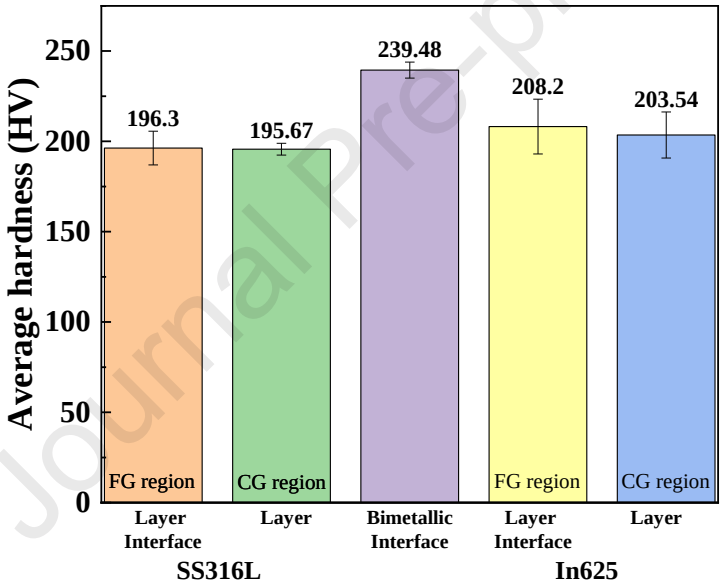

Figure 8. Location-specific average hardness on the SS316L, bimetallic interface, and In625 sides.

The tensile test results of the SS316L, In625, and bimetallic specimens are presented in **Figure 9(a)**. The bimetallic specimen exhibited a yield strength (YS) of approximately 400 MPa, an ultimate tensile strength (UTS) of 600 MPa, and an elongation of 40%. While the as-deposited SS316L displayed similar mechanical properties (YS: 410 MPa, UTS: 600 MPa, elongation: 40%), the In625 demonstrated higher strength and ductility (YS: 500 MPa, UTS: 650 MPa, elongation: 55%). Notably, UTS of the bimetallic specimen is similar to the as-deposited SS316L and the specimen failed on the SS316L side, as confirmed by the EDS analysis result in-set of **Figure 9(d)**.

Figures 9(b-d) show SEM images of the fractured surface of tensile specimen. The center and the edge region show predominantly dimple-like features, indicating a ductile fracture via the micro-void coalescence. Micro-voids nucleate at secondary

phase particles and coalesce to form larger voids, ultimately leading to fracture [12]. Equiaxed dimples in **Figures 9(b-d)-(i)** indicate uniaxial tensile stress is primarily dominant in these areas. Nevertheless, elongated dimples in **Figures 9(b-d)-(ii)** corroborate the presence of shear stress near the edges [12].

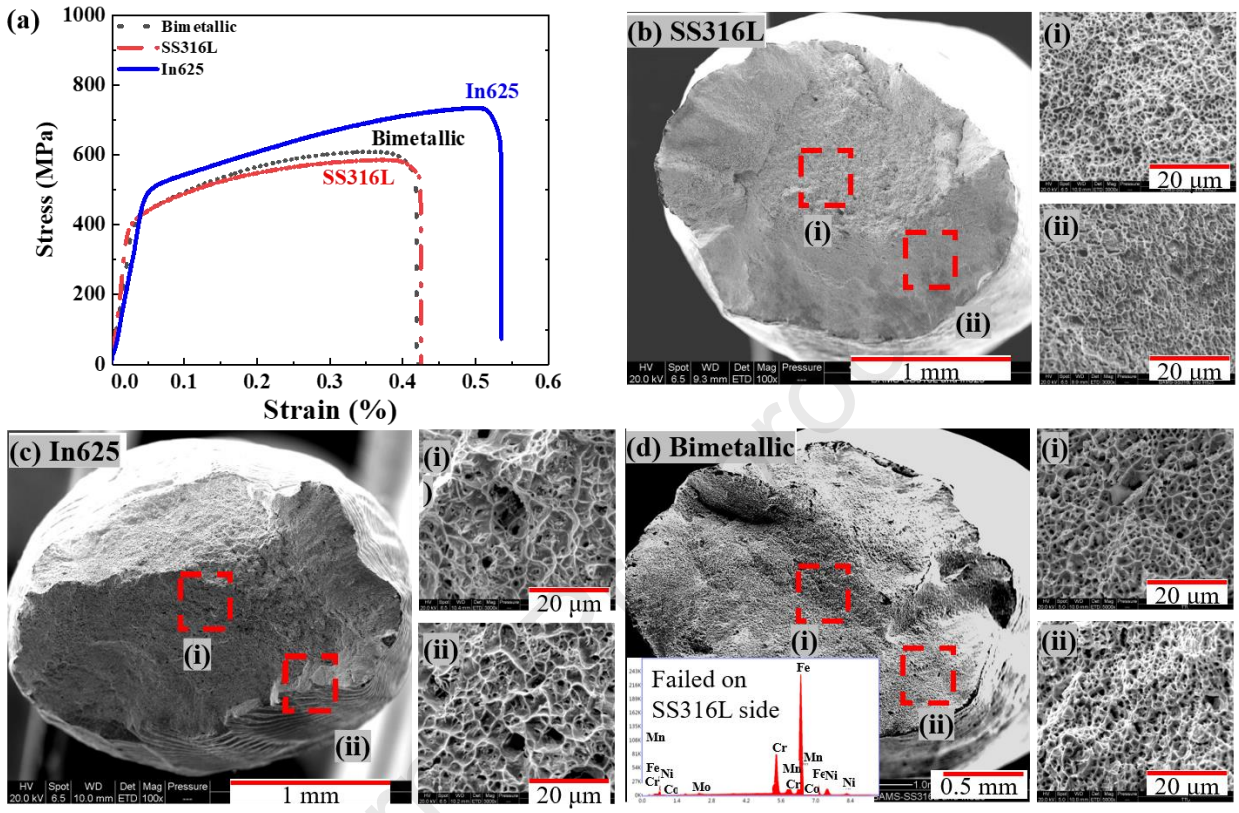

Figure 9. (a) stress vs. strain curves, (b-d) secondary electron SEM results from the fracture surface with a compositional analysis of the fracture surface of the bimetallic specimens inset of (d).

3.4. Digital image correlation (DIC)

The strain value obtained during the tensile test provides information on the overall gauge length (i.e., global strain). Hence, any local deviation in strain is averaged out and cannot be interpreted. In contrast, the strain response over a specific area can be analyzed using DIC as it measures strain response at pixel level. Therefore, DIC analysis is employed to investigate the influence of grain size on the local deformation phenomena and to quantify the material-specific deformation behavior of the bimetallic specimen.

DIC frames with 2-D strain maps along with local strain data on the marked location are presented in **Figure 10**. Periodically varied local strain values are observed on the SS316L and In625 tensile specimens, especially at higher deformations (total strain > 10%). To identify the locations of low and high local strains and correlate them with the grain size, tensile-tested samples were longitudinally cut through the middle using wire-EDM. By correlating the location-specific, cross-section diameter of tensile-deformed specimens, the layer interfaces (FG-regions) have less lateral deformation. Thus, the low-strain regions on the DIC strain maps are identified as the FG regions and vice versa. Later, virtual strain gauges are placed in these regions to extract the

quantitative local strain data, which is presented as the function of the global strain on the specimen (**Figure 10**). Both the SS316L and the In625 samples show low local strain values on the FG. It should also be noted that the span of low-strain regions in the *z*-direction (loading direction) is quite narrow as the FG regions are also significantly smaller than the CG regions. Similarly, virtual strain gauges are placed on the material-specific regions of the bimetallic specimen. The In625 side initially has up to a 25% overall strain, which is higher than the SS316L. Then, it gradually flattens and stabilizes to a constant value of ~30%. In contrast, the local strain on the SS316L side continues to increase at a higher rate. From the stain maps, it is apparent that the necking begins to occur in the SS316L at global strains of about 30%. Hence, the majority of the deformation is coming from the SS316L side after necking, which eventually leads to failure at this location.

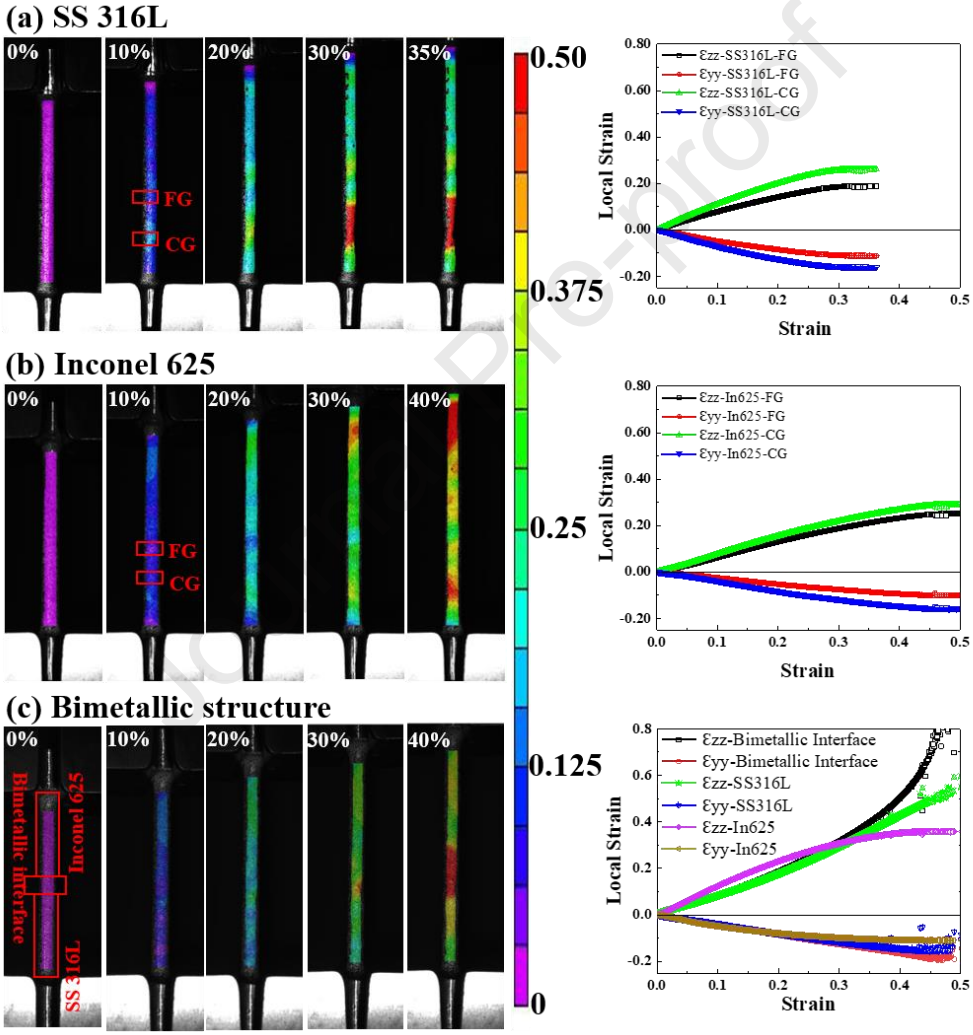

Figure 10. 2D-strain maps at varying global strain values along with plots showing the evolution of the local strain as a function of total (i.e., global) strain for (a) SS316L, (b) In625, and (c) bimetallic specimens.

One of the most important and widely used parameters for studying the formability and deformation mechanism is the *n*-value, which is the exponent of Hollomon's equation [46]:

$\sigma = K\epsilon^n$…… Eq. 10

where σ represents the applied true stress on the material, ϵ represents true strain, and *K* is the strength coefficient. From the DIC analyses, the longitudinal and lateral logarithmic (Hencky) strain data (ε_{zz} and ε_{yy}) at the FG and CG regions are extracted individually. Using the local lateral strain (ε_{yy}) and applied force data from the tensile tests, the local true stress is calculated. The values of the material and location-specific strength coefficients (*K*) are identified by extrapolating the true stress-strain data. Later, the strain-hardening exponent, *n*, is calculated using Eq. 1 and presented as a function of true strain in **Figure 11 (i-iii)**.

The effect of grain size on the work-hardening rate has been reported in prior works [46-47] based on the Hall-Petch relationship and suggests a higher work-hardening rate for smaller grain sizes. This trend is also evident in the present work. Both materials exhibit higher *n*-values at the FG regions as shown in **Figure 11**.

A low *n*-value signifies a high initial strain-hardening rate followed by a rapid decrease, whereas a high *n*-value indicates the opposite [48]. The material-specific local strain of the bimetallic specimen can be explained based on the *n*-values. The SS316L side has a lower *n*-value, and hence, has a higher initial strain-hardening rate, resulting in the initial low strain as observed in **Figure 11(iii)**. In contrast, the In625 has a higher *n*-value and a low initial work-hardening rate, which explains the higher initial strain. However, as the total deformation increases, the work hardening continues and gradually reduces the rate of deformation on the In625. Unlike the In625, the strain hardening rate of SS316L decreases at higher strain, resulting in higher deformation and eventual failure on this side.

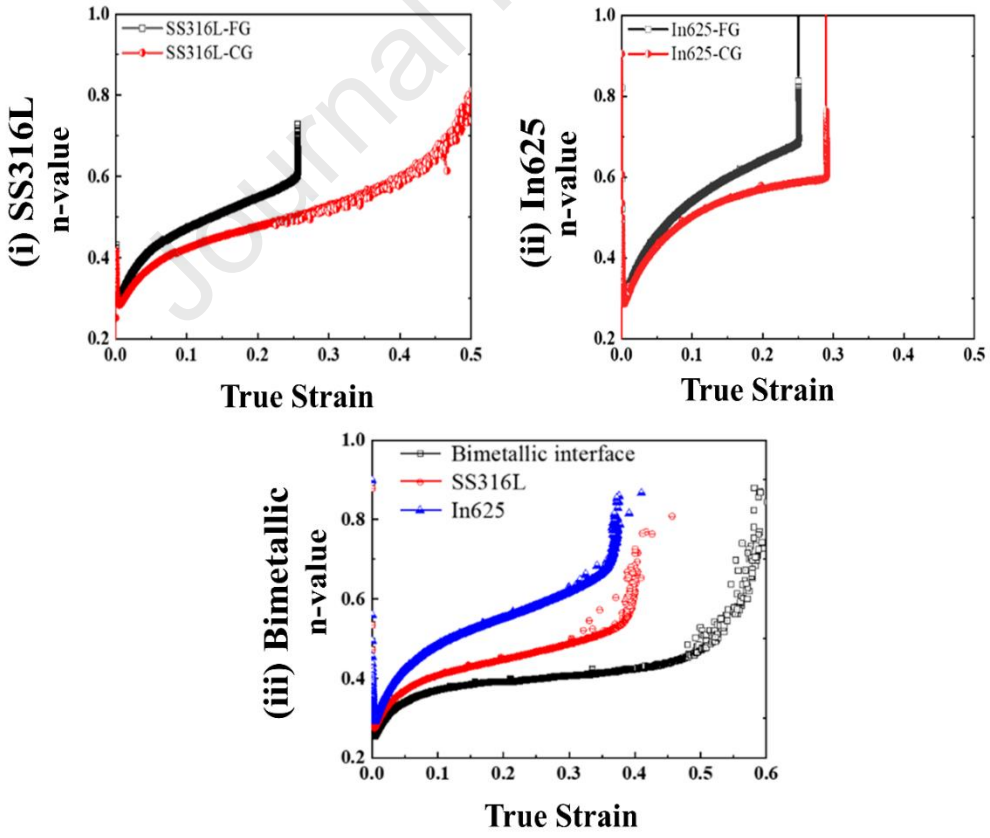

Figure 11. Calculated *n*-value on the marked locations in **Figure 10** for (i) SS316L, (ii) In625, and (iii) bimetallic specimens.

4. Discussion

4.1. Location of FG-regions and underlying mechanisms for CET

The FG regions are formed at the layer interface, which has been corroborated by microstructural analysis and hardness testing results. However, their position with respect to the FL has not been identified using the EBSD and DIC results. Based on research on GMAW, the finer grains are assumed to be formed at the recrystallized zone below the FL [26,49]. To verify the exact location of the FG regions, microhardness tests were performed at the layer interfaces over a 2 mm × 2 mm area for both materials, and the corresponding results are presented as contour maps in **Figure 12**. From the results, it is visible that the indents near the FL have the highest hardness in both materials. A higher magnification inspection of the highest hardness indents shows that the locations are right below the FL.

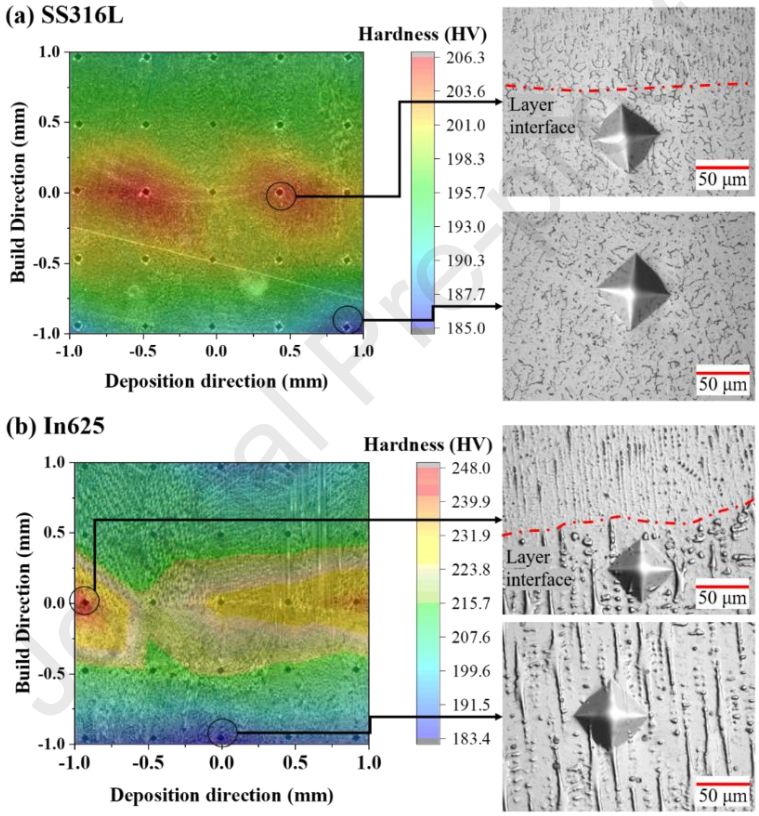

Figure 12. Hardness data on the layer interfaces of (a) SS316L and (b) In625 are plotted as contour maps with micrographs of the highest and lowest hardness indents.

Traditionally, the region below the FL with altered microstructure is identified as the heat-affected zone (HAZ), and the finer grain formation is attributed to the recrystallization in this region. The grain shape is correlated with the solidification parameters, and the *G*/*R* ratio is a critical parameter for determining grain morphology (columnar or equiaxed) [50]. As explained in prior work, a higher G/R ratio is associated with solidification front instability and columnar grain morphology [50].

The temperature distribution on the *xz*-plane of the FE model is presented in **Figure 13 (a-b)-(i)**. From the FE results, the temperatures at different distances from the top are recorded for a particular time frame and used for calculating the *G* utilizing Eq. 6 whereas, the slopes of the temperature vs. time curves at the same locations are calculated as R_c. Based on these calculated results, the *G*/*R* ratios at different

locations are calculated using Eq. 9 and presented in **Figure 13(a-b)-(ii)**. The *G*/*R* ratio is found to be highest near the top surface for both materials, which gradually decreases downwards. A sharp decrease in the *G*/*R* ratio is observed at about 3.5 mm from the surface, which is incidentally the region right below the FL (**Table 2:** layer thickness is 3 mm). Hence, this sharp decrease in the *G*/*R* ratio is correlated with the CET phenomenon and fine-grain formation in both materials.

It should be noted that previous literature strongly correlated the CET behavior and alloy composition due to the formation of the constitutional undercooled region ahead of the dendrite tips [30]. Data on the exact range for CET behavior of SS316L and In625 is not available in the literature and, hence, cannot be validated directly. However, the *G*/*R* values from the top section fall within the columnar region of the *G* vs. *R* graphs used in prior work [51] whereas, the values of the last four points in both materials (the region away from the top) fall within the transition zone.

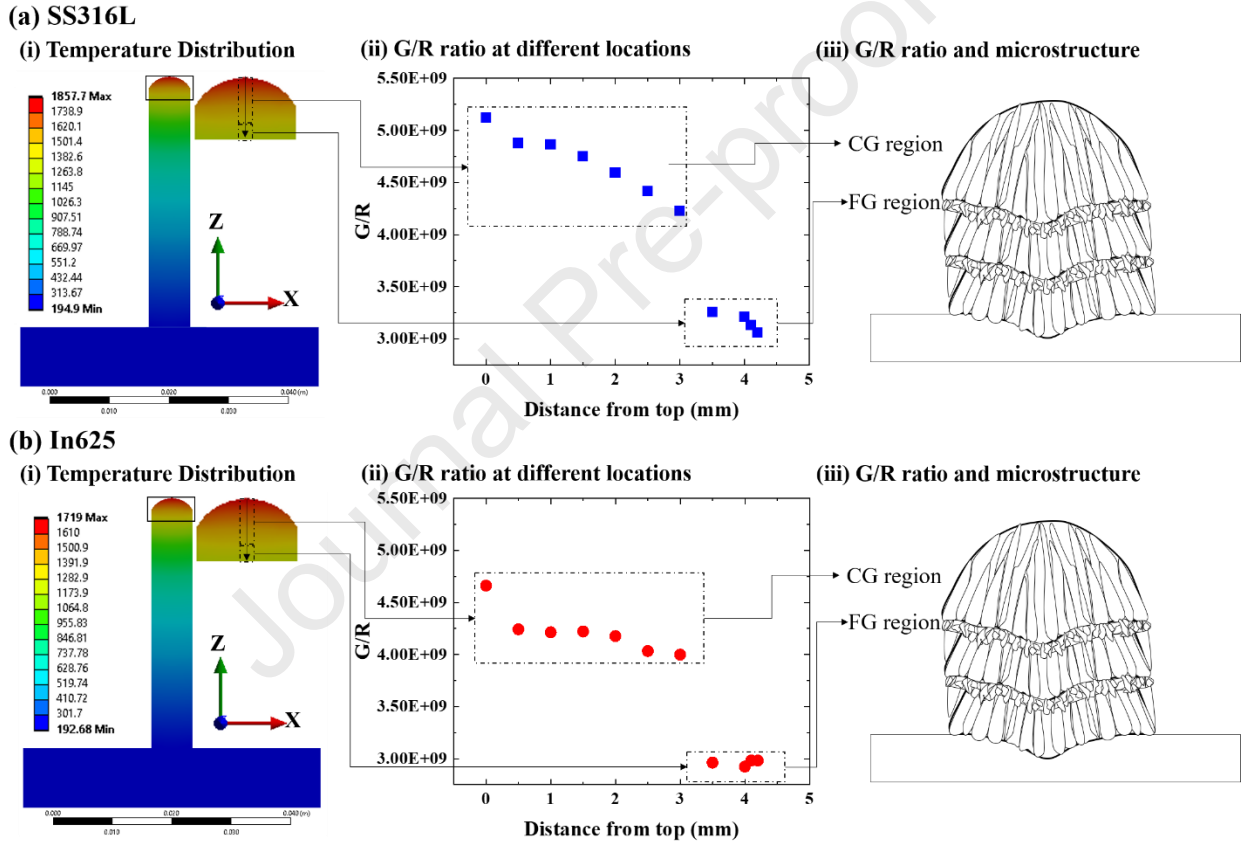

Figure 13. (i) Thermal map, (ii) *G*/*R* ratio, and (iii) Schematic representation of the microstructure for (a) SS316L and (b) In625.

The microstructural transformation right below the FL can be further confirmed by the microstructural features. As seen in **Figure 4(a)**, the layer interface has a lathy ferrite formation above the FL in SS316L. Whereas, the region between two-layer interfaces has mostly skeletal ferrite. The formation of lathy ferrite is associated with a faster cooling rate [41]. As stated earlier, an FA type of solidification is observed on the SS316L side. In such solidification, skeletal ferrites form with a moderate cooling rate whereas a high cooling rate leads to the formation of lathy ferrite [42]. As the region above the FL goes through rapid solidification, the formation of the lathy ferrite is observed in this region. However, the upper portion of a deposited layer goes through

much slower solidification and has mostly skeletal ferrite [52], as confirmed in fusion welding. The total ferrite content is also a function of the cooling rate and decreases with faster cooling [53]. The location-specific ferrite content data are presented in **Figure 14(a)**, showing the highest at regions away from the FL and lowest right above the FL, supporting the cooling rate dependency. However, the region right below the FL has reduced ferrite. It is assumed that this region is heated above the Austenitizing temperature during the deposition of the subsequent layer, and the ferrites get dissolved. The faster cooling rate further prohibits ferrite formation, reducing the total ferrite content. This also suggests that the temperature increases above the recrystallization temperature and finer grains form.

The microstructural transformation of In625 right below the FL can be validated based on the correlation between dendrite morphology, SDAS, and the cooling rate investigated in prior work [54]. The formation of columnar dendrites and secondary dendritic arms is associated with the cooling rate. The correlation between location-specific microstructure and cooling rate is schematically presented in **Figure 14(b)**. At the layer interface of the In625 (**Figures 4(c))**, the region right above the FL has a shorter dendritic growth with almost no secondary dendritic arms due to the faster solidification. A location away from the FL has visible columnar dendritic growth with secondary arms on almost every dendrite. The SDAS is measured at 7.70 µm on average. At the region below the FL, the dendrites are shortened, and fewer of them have secondary arms with lower SDAS (6.04 µm on average). As the correlation between cooling rate and SDAS is inversely proportional as schematically presented in **Figure 14(b)** [54], the lower SDAS at the region right below the FL suggests a faster solidification at this region.

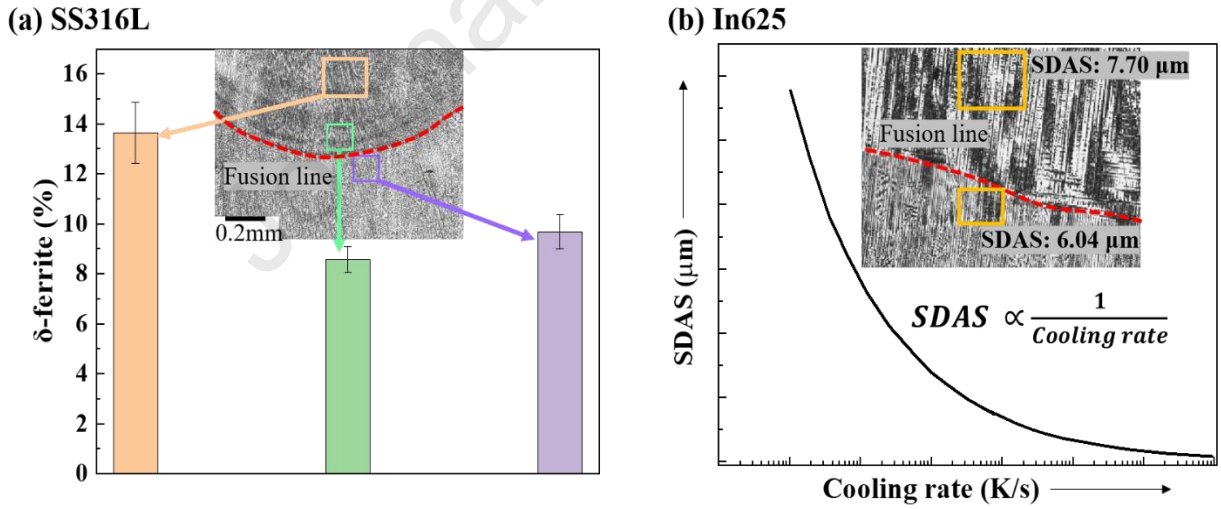

Figure 14. (a) Location-specific ferrite content on SS316L and (b) SDAS vs. cooling rate graph reproduced from [48] with micrograph from a layer interface with SDAS value measured.

4.2. Grain size and deformation

Dislocation movement is the primary mechanism enabling plastic deformation in metals. Hindering dislocation motion is crucial for many strengthening mechanisms, including grain boundary strengthening. During the deformation of polycrystals, a strain gradient is required to maintain the compatibility at grain boundaries because different directionality of slip systems in adjacent grains (due to different grain

orientations) causes local plastic heterogeneity [55]. Among the dislocations, the geometrically necessary dislocations (GNDs) arise due to the presence of strain gradient, leading to the rotation in continuum field and the overall Burgers vector [56]. During non-homogenous deformation of polycrystals, GNDs influence work hardening [57-58] and can contribute to further hardening [57]. In this regard, EBSD analysis can detect the collective effects of dislocations accumulated in the lattice during deformation as GND density maps. GNDs are more likely to accumulate at the grain boundaries, and the GND density tends to be higher in smaller grains [59]. Hence, the GND density maps can correlate the grain size effect on the plastic deformation of the crystallite lattice [56].

To correlate the material and grain size with the local plastic deformation behavior, EBSD analysis was performed on a tensile-interrupted bimetallic sample. The GND density maps of the unstressed and stressed specimen (FG and CG regions from SS316L and Inconel625 sides, and bimetallic interface) are presented in **Figure 15**. In unstressed conditions, none of the specimens show any significant GND density or variation, depending on the grain size or composition (**Figures 15(a-c)-(i)**). However, once plastically deformed, the effects become more visible as can be seen in **Figures 15(ii-iii)**. Both for SS316L and In625 sides of the bimetallic specimen, the GND density is higher at the FG region. Even though a higher deformation is found at the CG regions of both materials in DIC analysis (**Figure 11**), the GND density is lower. This difference in deformation and GND density is attributed to the dislocation motion and grain boundary interaction. The FG region has a higher density of grain boundaries, which act as deterrents to the dislocation motion necessary to accommodate slip. Dislocation accumulation at the grain boundaries results in local plastic heterogeneity, which leads to higher GND density whereas, in the CG region, the fraction of GBs occupying the total volume fraction is significantly lower. As a result, dislocation motion is comparatively easier and increases the GND density.

Once stressed, the In625 side shows comparatively higher GND density at the bimetallic interface (**Figure 15(c)**). This phenomenon can also be correlated with the strain hardening coefficient in **Figure 11(iii)**. A higher dislocation density is often associated with a higher strain hardening rate [61] and is observed in the FG and CG regions. The FG regions have a higher strain-hardening rate for both materials, and the GND density is also higher. On the bimetallic specimen, a higher strain-hardening coefficient is calculated on In625, and the GND density is also found to be higher on this side.

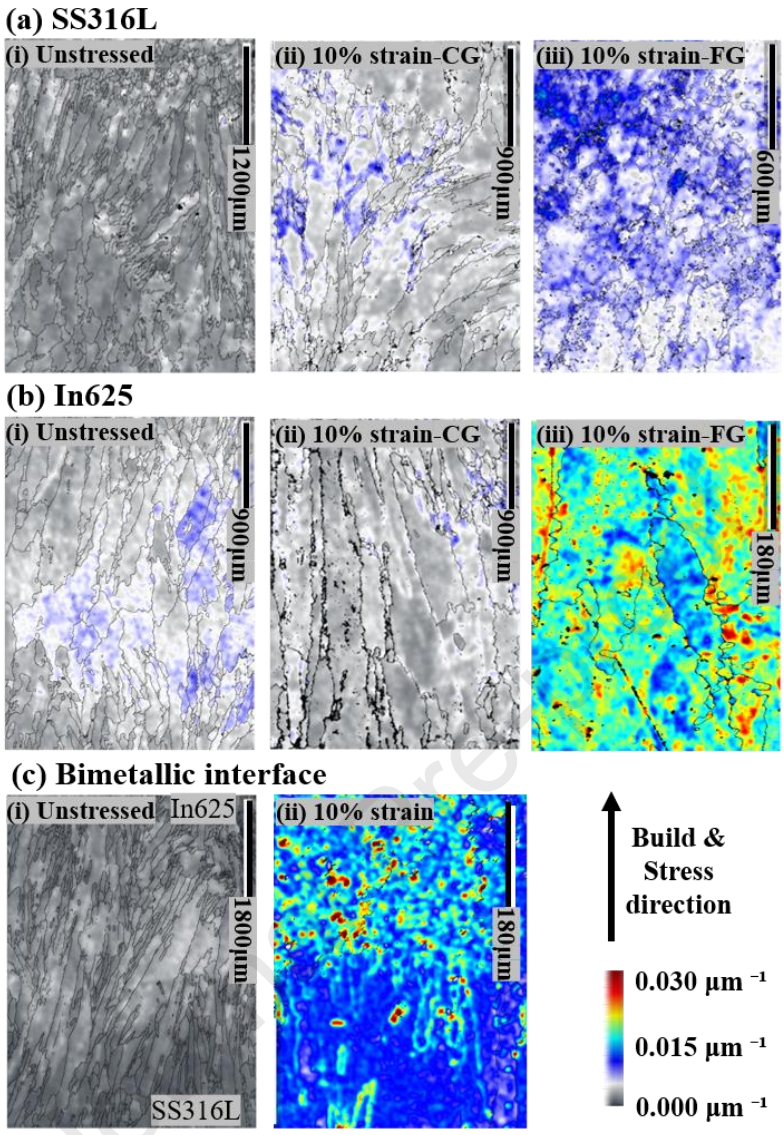

Figure 15. Geometrically necessary dislocation (GND) density data are color-coded within the same range from the (a) SS316L and (b) In625 sides as well as the (c) bimetallic interface before and after applying stress.

4.3. Improvement of mechanical properties

In this section, the uniaxial tensile test results of CDS from the authors' previous works [13,33] are compared against the IDS used in this work and presented in **Figure 16**. In both materials and the bimetallic structure, the IDS results in improved yield performance and ductility. The YS is improved by 42.5%, 23.6%, and 24.9% in SS316L, In625, and bimetallic specimens, respectively. The increase in YS is attributed to the grain size difference between the two deposition strategies. Due to the alternating and overall smaller grain size, the Hall-Petch effect contributes to the improved strength of the specimen.

The elongation is improved by 120% and 43% in the SS316L and bimetallic specimens, respectively. The improved ductility in both cases is attributed to the difference in δ-ferrite content. The CDS leads to temperature build-up as well as slower cooling. This results in a much higher δ-ferrite content as apparent from

Figures 16(b-c)-(i), which reduces the ductility. The improved ductility of the bimetallic specimen also comes from the SS316L side as most of the deformation occurs on this material. In625 does not show much difference in elongation as the microstructural features are similar in both.

The difference in cooling rate between the two deposition strategies is also apparent from the In625 microstructure (**Figures 16(b-c)-(ii)**). The primary and secondary dendrite arm spacing (PDAS and SDAS) in nickel alloys is inversely correlated to the cooling rate [54,62]. The higher PDAS and SDAS values in CDS indicate a slower cooling rate and corroborate the larger grain formation.

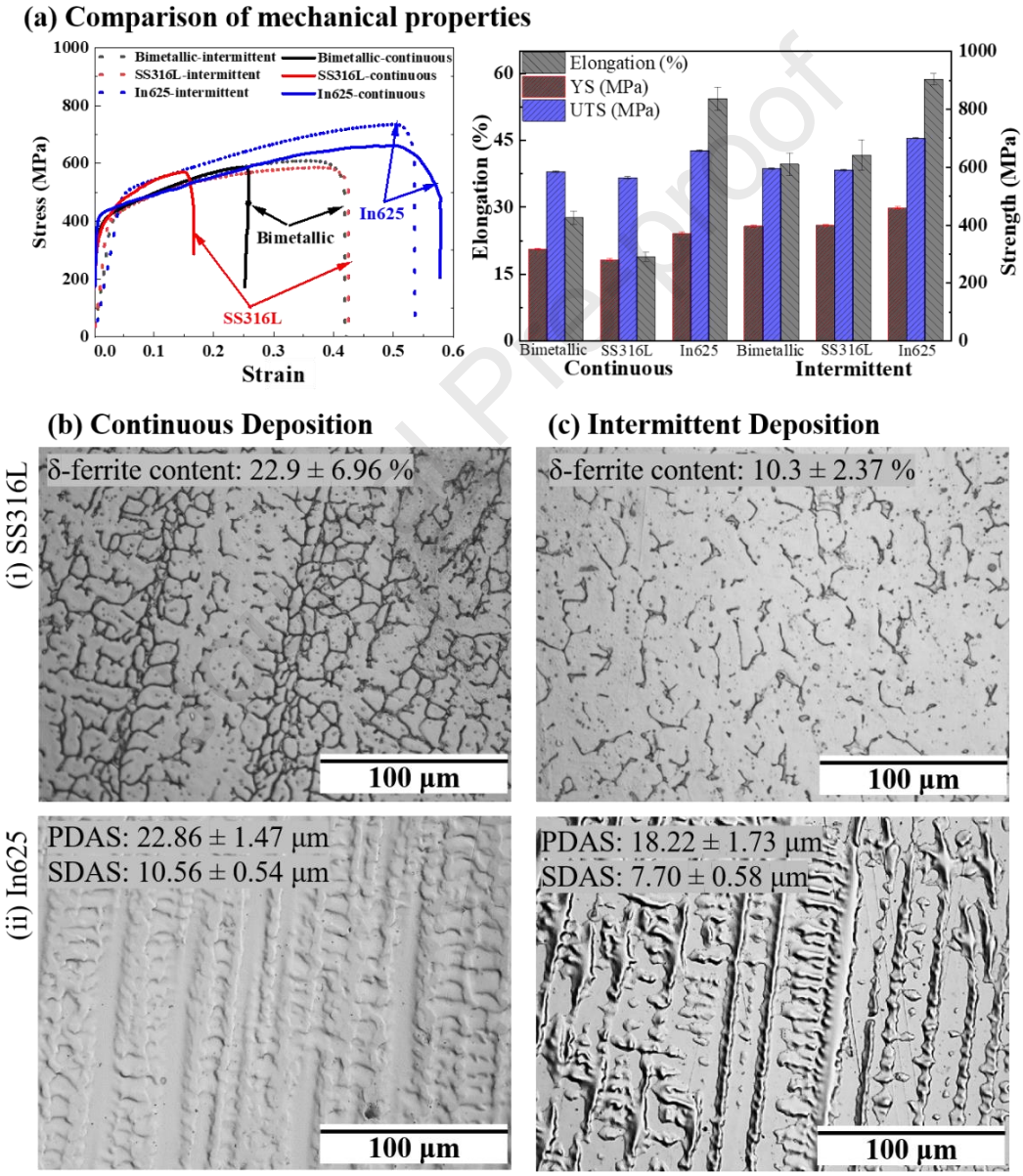

Figure 16. Comparison of (a) mechanical properties and (b-c) microstructure between CDS and IDS.

5. Conclusions

In this work, a controlled periodically alternating grain size is attained by promoting columnar to equiaxed transition (CET) through an intermittent deposition strategy in the bimetallic structure of two FCC materials, SS316L and In625. The microstructure and mechanical behaviors of microstructurally graded as well as compositionally graded bimetallic structures were investigated. Strain mapping throughout the uniaxial tensile test provided an in-situ perspective of the heterogeneous deformations in response to microstructural and/or compositional heterogeneity.

Based on the evidence and results, the following conclusions are drawn:

- During the deposition of a layer, a part of the previous layer right below the fusion line goes through recrystallization with a lower G/R ratio, which promotes CET in this region and results in smaller and equiaxed grains. The lower G/R ratio in the region right below the fusion line is validated through a thermal model.
- The grain size modification is further confirmed by the microstructural attributes: the ferrite content and morphology on SS316L, and the SDAS on In625, respectively. The formation of lathy δ-ferrite, as well as reduced ferrite content, are associated with a faster solidification in SS316L, and the region right below the FL meets both criteria. On the other hand, higher SDAS on In625 is correlated with a higher cooling rate and is measured right below the FL. These correlations suggest that the region below the FL goes through recrystallization with a CET.
- As a result of CET, a difference in local strain is observed in both materials during the tensile test. The CG regions go through higher deformation under the same applied force whereas, the FG regions have a higher strain hardening rate due to the Hall-Petch effect. The GND maps from tensile-interrupted specimens also show higher GND density at the FG region, confirming the strain hardening.
- Although the In625 side of the bimetallic specimen goes through higher deformation at the beginning, the rate of deformation eventually subsides due to the higher strain-hardening rate, which is also supported by the GND density analysis of the EBSD results.
- The periodically alternating grain size facilitated by the intermittent deposition strategy results in a faster cooling rate of each layer as well as interrupted grain growth. The faster cooling rate results in a lower ferrite content in the SS316L (~22% in continuous vs. ~10% in intermittent deposition), resulting in a higher ductility in the SS316L and bimetallic specimens whereas the alternating and overall smaller grain size improves the strength of the In625. The bimetallic specimen with intermittent deposition shows higher strength and ductility.

6. Acknowledgments

The authors of this paper appreciate the continuous support provided by the Center for Manufacturing Research (CMR) and the Department of Manufacturing and Engineering Technology at Tennessee Technological University. This material is based upon work supported by the National Science Foundation under Grant No. 2015693. The authors would like to thank Dr. Philip Barnett for his assistance with the

DIC setup. The authors would like to acknowledge support by the US Department of Energy, Office of Energy Efficiency and Renewable Energy, Advanced Manufacturing Office, under contract DE-AC05-00OR22725 with UT-Battelle, LLC. APT research was supported by the Center for Nanophase Materials Sciences (CNMS), which is a US Department of Energy, Office of Science User Facility at Oak Ridge National Laboratory. This work was supported by the National Research Foundation of Korea (NRF) grant funded by the Korea government (MSIT) (No. RS-2024-00346883). The authors would like to thank James Burns for his assistance in performing APT sample preparation and running the APT experiments.

7. References

[1] A. Bhatia, A.K. Sehgal, Additive manufacturing materials, methods and applications: A review, Materials Today: Proceedings, 81 (2023) 1060–1067. doi.org/10.1016/j.matpr.2021.04.379.

[2] M. Srivastava, S. Rathee, A. Tiwari, M. Dongre, Wire arc additive manufacturing of metals: A review on processes, materials and their behaviour. Materials Chemistry and Physics, 294 (2023),126988. doi.org/10.1016/j.matchemphys.2022.126988.

[3] H. Yi, L. Jia, J. Ding, H. Li, Achieving material diversity in wire arc additive manufacturing: Leaping from alloys to composites via wire innovation. International Journal of Machine Tools and Manufacture, 194 (2024),104103. doi.org/10.1016/j.ijmachtools.2023.104103.

[4] Z. Ma, W. Liu, W. Li, H. Liu, J. Song, Y. Liu, Y. Huang, Y. Xia, Z. Wang, B. Liu, Z. Lv, G. Hu, T. Wang, T. Li, S. Liu, Y. Zhang, Additive manufacturing of functional gradient materials: A review of research progress and challenges. Journal of Alloys and Compounds, (2024)172642. doi.org/10.1016/j.jallcom.2023.172642.

[5] B.E. Carroll, R.A. Otis, J.P. Borgonia, J. Suh, R.P. Dillon, A.A. Shapiro, D.C. Hofmann, Z.-K. Liu, A.M. Beese, Functionally graded material of 304L stainless steel and inconel 625 fabricated by directed energy deposition: Characterization and thermodynamic modeling, Acta Mater. 19 (2016) 46–54. doi:10.1016/j.actamat.2016.02.019.

[6] L.D. Bobbio, R.A. Otis, J.P. Borgonia, R.P. Dillon, A.A. Shapiro, Z.K. Liu, A.M. Beese, Additive manufacturing of a functionally graded material from Ti-6Al-4V to Invar: Experimental characterization and thermodynamic calculations, Acta Mater. 127 (2017) 133–142. doi:10.1016/j.actamat.2016.12.070.

[7] B. Onuike, A. Bandyopadhyay, Bond strength measurement for additively manufactured Inconel 718- GRCop84 copper alloy bimetallic joints, Addit. Manuf. 27 (2019) 576–585. doi:10.1016/j.addma.2019.04.003.

[8] B. Onuike, A. Bandyopadhyay, Additive manufacturing of Inconel 718 – Ti6Al4V bimetallic structures, Addit. Manuf. 22 (2018) 844–851. doi:10.1016/j.addma.2018.06.025.

[9] M.R.U. Ahsan, X. Fan, G.-J.G.J. Seo, C. Ji, M. Noakes, A. Nycz, P.K. Liaw, .D.B. Kim, Microstructures and mechanical behavior of the bimetallic additively-manufactured structure (BAMS) of austenitic stainless steel and Inconel 625, J. Mater. Sci. Technol. 74 (2021) 176–188. doi:10.1016/j.jmst.2020.10.001.

[10] M.R.U. Ahsan, A.N.M. Tanvir, G.-J. Seo, B. Bates, W. Hawkins, C. Lee, P.K. Liaw, M. Noakes, A. Nycz, D.B. Kim, Heat-treatment effects on a bimetallic additively-manufactured structure (BAMS) of the low-carbon steel and

austenitic-stainless steel, Addit. Manuf. 32 (2020) 101036. doi:10.1016/j.addma.2020.101036.

[11] B. Wu, Z. Pan, D. Ding, D. Cuiuri, H. Li, J. Xu, J. Norrish, A review of the wire arc additive manufacturing of metals: properties, defects and quality improvement, J. Manuf. Process. 35 (2018) 127–139. doi:10.1016/j.jmapro.2018.08.001.

[12] T. Abe, H. Sasahara, Dissimilar metal deposition with a stainless steel and nickel-based alloy using wire and arc-based additive manufacturing, Precis. Eng. 45 (2016) 387–395. doi:http://dx.doi.org/10.1016/j.precisioneng.2016.03.016.

[13] M.R.U. Ahsan, A.N.M. Tanvir, T. Ross, A. Elsawy, M.-S. Oh, D.B. Kim, Fabrication of bimetallic additively manufactured structure (BAMS) of low carbon steel and 316L austenitic stainless steel with wire + arc additive manufacturing, Rapid Prototyp. J. 26 (2019) 519-530. doi:10.1108/RPJ-09-2018-0235.

[14] Z. Sun, X.P. Tan, M. Descoins, D. Mangelinck, S.B. Tor, C.S. Lim, Revealing hot tearing mechanism for an additively manufactured high-entropy alloy via selective laser melting, Scr. Mater. 168 (2019) 129–133. doi:10.1016/j.scriptamat.2019.04.036.

[15] Y.S.J. Yoo, T.A. Book, M.D. Sangid, J. Kacher, Identifying strain localization and dislocation processes in fatigued Inconel 718 manufactured from selective laser melting, Mater. Sci. Eng. A. 724 (2018) 444–451. doi:10.1016/j.msea.2018.03.127.

[16] X. Chen, J. Li, X. Cheng, H. Wang, Z. Huang, Effect of heat treatment on microstructure, mechanical and corrosion properties of austenitic stainless steel 316L using arc additive manufacturing, Mater. Sci. Eng. A. 715 (2018) 307–314. doi:10.1016/j.msea.2017.10.002.

[17] Tripathi, U., Saini, N., Mulik, R.S. and Mahapatra, M.M., Effect of build direction on the microstructure evolution and their mechanical properties using GTAW based wire arc additive manufacturing. CIRP Journal of Manufacturing Science and Technology, 37 (2022*)*, pp.103-109. doi.org/10.1016/j.cirpj.2022.01.010.

[18] N. Sargent, M. Jones, R. Otis, A.A. Shapiro, J.P. Delplanque, W. Xiong, Integration of processing and microstructure models for non-equilibrium solidification in additive manufacturing, Metals (Basel). 11 (2021) 1–12. doi:10.3390/met11040570.

[19] L. Yuan, A.S. Sabau, D. Stjohn, A. Prasad, P.D. Lee, Columnar-to-equiaxed transition in a laser scan for metal additive manufacturing, IOP Conf. Ser. Mater. Sci. Eng. 861 (2020) 012007. doi:10.1088/1757-899X/861/1/012007.

[20] P.A. Morton, J. Mireles, H. Mendoza, P.M. Cordero, M. Benedict, R.B. Wicker, Enhancement of low-cycle fatigue performance from tailored microstructures enabled by electron beam melting additive manufacturing technology, J. Mech. Des. Trans. ASME. 137 (2015) 2015–2018. doi:10.1115/1.4031057.

[21] N. Raghavan, B.C. Stump, P. Fernandez-Zelaia, M.M. Kirka, S. Simunovic, Influence of geometry on columnar to equiaxed transition during electron beam powder bed fusion of IN718, Addit. Manuf. (2021) 102209. doi:10.1016/j.addma.2021.102209.

[22] V.A. Popovich, E. V. Borisov, A.A. Popovich, V.S. Sufiiarov, D. V. Masaylo, L. Alzina, Functionally graded Inconel 718 processed by additive manufacturing: Crystallographic texture, anisotropy of microstructure and mechanical properties, Mater. Des. 114 (2017) 441–449. doi:10.1016/j.matdes.2016.10.075.

[23] F. Wang, S. Williams, M. Rush, Morphology investigation on direct current pulsed gas tungsten arc welded additive layer manufactured Ti6Al4V alloy, Int. J. Adv. Manuf. Technol. 2011 575. 57 (2011) 597–603. doi:10.1007/S00170-011-3299-1.

[24] A.S. Yildiz, K. Davut, B. Koc, O. Yilmaz, Wire arc additive manufacturing of high-strength low alloy steels: Study of process parameters and their influence on the bead geometry and mechanical characteristics, Int. J. Adv. Manuf. Technol. 108 (2020) 3391–3404. doi:10.1007/s00170-020-05482-9.

[25] C.E. Seow, H.E. Coules, G. Wu, R.H.U. Khan, X. Xu, S. Williams, Wire + arc additively manufactured Inconel 718: Effect of post-deposition heat treatments on microstructure and tensile properties, Mater. Des. 183 (2019) 108157. doi:10.1016/J.MATDES.2019.108157.

[26] Z.Z. Zhang, C.S. Wu, Monte Carlo simulation of grain growth in heat-affected zone of 12 wt.% Cr ferritic stainless steel hybrid welds, Comput. Mater. Sci. 65 (2012) 442–449. doi:10.1016/J.COMMATSCI.2012.07.040.

[27] M. Benakis, D. Costanzo, A. Patran, Current mode effects on weld bead geometry and heat affected zone in pulsed wire arc additive manufacturing of Ti-6-4 and Inconel 718, J. Manuf. Process. 60 (2020) 61–74. doi:10.1016/J.JMAPRO.2020.10.018.

[28] A. Prasad, L. Yuan, P. Lee, M. Patel, D. Qiu, M. Easton, D. St. John, Towards understanding grain nucleation under additive manufacturing solidification conditions, Acta Mater. 195 (2020) 392–403. doi:10.1016/j.actamat.2020.05.012.

[29] Y.J. Liang, X. Cheng, J. Li, H.M. Wang, Microstructural control during laser additive manufacturing of single-crystal nickel-base superalloys: New processing-microstructure maps involving powder feeding, Mater. Des. 130 (2017) 197–207. doi:10.1016/j.matdes.2017.05.066.

[30] M. Haines, A. Plotkowski, C.L. Frederick, E.J. Schwalbach, S.S. Babu, A sensitivity analysis of the columnar-to-equiaxed transition for Ni-based superalloys in electron beam additive manufacturing, Comput. Mater. Sci. 155 (2018) 340–349. doi:10.1016/j.commatsci.2018.08.064.

[31] A.N.M. Tanvir, M.R.U. Ahsan, G. Seo, B. Bates, C. Lee, P.K. Liaw, M. Noakes, A. Nycz, C. Ji, D.B. Kim, Phase stability and mechanical properties of wire + arc additively manufactured H13 tool steel at elevated temperatures, J. Mater. Sci. Technol. 67 (2021) 80-94. doi:10.1016/j.jmst.2020.04.085.

[32] A.N.M. Tanvir, M.R.U. Ahsan, C. Ji, W. Hawkins, B. Bates, D.B. Kim, Heat treatment effects on Inconel 625 components fabricated by wire + arc additive manufacturing (WAAM)-part 1: microstructural characterization, Int. J. Adv. Manuf. Technol. 103 (2019) 3785-3798. doi:10.1007/s00170-019-03828-6.

[33] A.N.M. Tanvir, M.R.U. Ahsan, G. Seo, J. duk Kim, C. Ji, B. Bates, Y. Lee, D.B. Kim, Heat treatment effects on Inconel 625 components fabricated by wire + arc additively manufacturing (WAAM)—part 2: mechanical properties, Int. J. Adv. Manuf. Technol. 110 (2020) 1709–1721. doi:10.1007/s00170-020-05980-w.

[34] B.L. Bramfitt, A.O. Benscoter, Metallographer's guide practices and procedures for irons and steels, ASM International, 2002. https://www.asminternational.org/.

[35] K. Thompson, D. Lawrence, D.J. Larson, J.D. Olson, T.F. Kelly, B. Gorman, In situ site-specific specimen preparation for atom probe tomography, Ultramicroscopy. 107 (2007) 131–139. doi:10.1016/j.ultramic.2006.06.008.

[36] B. Beausir, J.-J. Fundenberger, Analysis Tools for Electron and X-ray diffraction, ATEX - software, www.atex-software.eu, Université de Lorraine - Metz., (2017).

http://www.atex-software.eu/help.html.
[37] ASTM International, Standard Test Methods for Tension Testing of Metallic Materials 1, i (2004) 1–25.
[38] X. Zhan, X. Lin, Z. Gao, C. Qi, J. Zhou, D. Gu, Modeling and simulation of the columnar-to-equiaxed transition during laser melting deposition of Invar alloy, J. Alloys Compd. 755 (2018) 123–134. doi:10.1016/j.jallcom.2018.04.313.
[39] Gupta, D.K. and Mulik, R.S., Numerical simulation and experimental investigation of temperature distribution during the wire arc additive manufacturing (WAAM) process. *Progress in Additive Manufacturing*, (2024),pp 1-15. doi.org/10.1007/s40964-024-00647-4
[40] L. Wang, J. Xue, Q. Wang, Correlation between arc mode, microstructure, and mechanical properties during wire arc additive manufacturing of 316L stainless steel, Mater. Sci. Eng. A. 751 (2019) 183–190. doi:10.1016/j.msea.2019.02.078.
[41] H. Inoue, T. Koseki, S. Ohkita, M. Fuji, Formation mechanism of vermicular and lacy ferrite in austenitic stainless steel weld metals, Sci. Technol. Weld. Join. 5 (2000) 385–396. doi:10.1179/136217100101538452.
[42] J.C. Lippold, D.J. Kotecki, Welding Metallurgy and Weldability of Stainless Steels, John Wiley & Sons, 2005. doi:10.1002/9781118960332.
[43] B.K. Foster, Characterization of Inconel® 625 and Ti-6Al-4V Laser Deposited Builds Manufactured with Varying Dwell Times, 2015.
[44] H. Naffakh, M. Shamanian, F. Ashrafizadeh, Microstructural evolutions in dissimilar welds between AISI 310 austenitic stainless steel and Inconel 657, J. Mater. Sci. 45 (2010) 2564–2573. doi:10.1007/s10853-010-4227-8.
[45] J. Rodriguez, K. Hoefer, A. Haelsig, P. Mayr, Functionally graded SS 316L to Ni-based structures produced by 3D plasma metal deposition, Metals (Basel). 9 (2019) 620. doi:10.3390/met9060620.
[46] H.J. Kleemola, M.A. Nieminen, On the strain-hardening parameters of metals., Met. Trans. 5 (1974) 1863–1866. doi:10.1007/BF02644152.
[47] M. Opiela, G. Fojt-Dymara, A. Grajcar, W. Borek, Effect of grain size on the microstructure and strain hardening behavior of solution heat-treated low-C high-Mn steel, Materials (Basel). 13 (2020). doi:10.3390/MA13071489.
[48] J. George, E. Deiter, Mechanical metallurgy, McGraw-Hill Book Company, 1961.
[49] H.L. Wei, J.W. Elmer, T. DebRoy, Three-dimensional modeling of grain structure evolution during welding of an aluminum alloy, Acta Mater. 126 (2017) 413–425. doi:10.1016/J.ACTAMAT.2016.12.073.
[50] S. Paul, J. Liu, S.T. Strayer, Y. Zhao, S. Sridar, M.A. Klecka, W. Xiong, A.C. To, A discrete dendrite dynamics model for epitaxial columnar grain growth in metal additive manufacturing with application to Inconel, Addit. Manuf. 36 (2020) 101611. doi:10.1016/j.addma.2020.101611.
[51] H. Li, Y. Huang, S. Jiang, Y. Lu, X. Gao, X. Lu, Z. Ning, J. Sun, Columnar to equiaxed transition in additively manufactured CoCrFeMnNi high entropy alloy, Mater. Des. 197 (2021). doi:10.1016/j.matdes.2020.109262.
[52] J.A. Brooks, N.C.Y. Yang, J.S. Krafcik, Clarification on development of skeletal and lathy ferrite morphologies in stainless steel welds, Sci. Technol. Weld. Join. 6 (2001) 412–414. doi:10.1179/stw.2001.6.6.412.
[53] J.W. Elmer, S.M. Allen, T.W. Eagar, The influence of cooling rate on ferrite content of stainless steel alloys, Proc. 2nd Int. Conf. Trends Weld. Res. (1989) 165–170.
[54] J. Tinoco, H. Fredriksson, Solidification of a modified Inconel 625 alloy under different cooling rates, High Temp. Mater. Process. 23 (2004) 13–24.

doi:10.1515/HTMP.2004.23.1.13.
[55] L.T. Hansen, D.T. Fullwood, E.R. Homer, R.H. Wagoner, H. Lim, J.D. Carroll, G. Zhou, H.J. Bong, An investigation of geometrically necessary dislocations and back stress in large grained tantalum via EBSD and CPFEM, Mater. Sci. Eng. A. 772 (2020) 138704. doi:10.1016/j.msea.2019.138704.
[56] L.N. Brewer, D.P. Field, C.C. Merriman, Mapping and assessing plastic deformation using EBSD, Electron Backscatter Diffr. Mater. Sci. (2009) 251–262. doi:10.1007/978-0-387-88136-2_18.
[57] H. Gao, Y. Huang, Geometrically necessary dislocation and size-dependent plasticity, Scr. Mater. 48 (2003) 113–118. doi:10.1016/S1359-6462(02)00329-9.
[58] S. Zhang, W. Liu, J. Wan, R.D.K. Misra, Q. Wang, C. Wang, The grain size and orientation dependence of geometrically necessary dislocations in polycrystalline aluminum during monotonic deformation: Relationship to mechanical behavior, Mater. Sci. Eng. A. 775 (2020) 138939. doi:10.1016/J.MSEA.2020.138939.
[59] L.P. Kubin, A. Mortensen, Geometrically necessary dislocations and strain-gradient plasticity: A few critical issues, Scr. Mater. 48 (2003) 119–125. doi:10.1016/S1359-6462(02)00335-4.
[60] S. Zhang, W. Liu, J. Wan, R.D.K. Misra, Q. Wang, C. Wang, The grain size and orientation dependence of geometrically necessary dislocations in polycrystalline aluminum during monotonic deformation: Relationship to mechanical behavior, Mater. Sci. Eng. A. 775 (2020) 138939. doi:10.1016/J.MSEA.2020.138939.
[61] B. Viguier, Dislocation densities and strain hardening rate in some intermetallic compounds, Mater. Sci. Eng. A. 349 (2003) 132–135. doi:10.1016/S0921-5093(02)00785-2.
[62] Y. Zhang, B. Huang, J. Li, Microstructural evolution with a wide range of solidification cooling rates in a Ni-based superalloy, Metall. Mater. Trans. A Phys. Metall. Mater. Sci. 44 (2013) 1641–1644. doi:10.1007/s11661-013-1645-7.

Declaration of interests

☒ The authors declare that they have no known competing financial interests or personal relationships that could have appeared to influence the work reported in this paper.

☐The authors declare the following financial interests/personal relationships which may be considered as potential competing interests: